

POST-OUTBURST X-RAY FLUX AND TIMING EVOLUTION OF SWIFT J1822.3–1606

P. SCHOLZ, C.-Y. NG, M. A. LIVINGSTONE, V. M. KASPI, A. CUMMING, AND R. F. ARCHIBALD

Department of Physics, Rutherford Physics Building, McGill University, 3600 University Street, Montreal, Quebec H3A 2T8, Canada; pscholz@physics.mcgill.ca

Received 2012 April 4; accepted 2012 October 25; published 2012 November 21

ABSTRACT

Swift J1822.3–1606 was discovered on 2011 July 14 by the *Swift* Burst Alert Telescope following the detection of several bursts. The source was found to have a period of 8.4377 s and was identified as a magnetar. Here we present a phase-connected timing analysis and the evolution of the flux and spectral properties using *Rossi X-ray Timing Explorer*, *Swift*, and *Chandra* observations. We measure a spin frequency of $0.1185154343(8) \text{ s}^{-1}$ and a frequency derivative of $-4.3 \pm 0.3 \times 10^{-15}$ at MJD 55761.0, in a timing analysis that includes significant non-zero second and third frequency derivatives that we attribute to timing noise. This corresponds to an estimated spin-down inferred dipole magnetic field of $B \sim 5 \times 10^{13} \text{ G}$, consistent with previous estimates though still possibly affected by unmodeled noise. We find that the post-outburst 1–10 keV flux evolution can be characterized by a double-exponential decay with decay timescales of 15.5 ± 0.5 and 177 ± 14 days. We also fit the light curve with a crustal cooling model, which suggests that the cooling results from heat injection into the outer crust. We find that the hardness–flux correlation observed in magnetar outbursts also characterizes the outburst of Swift J1822.3–1606. We compare the properties of Swift J1822.3–1606 with those of other magnetars and their outbursts.

Key words: pulsars: individual (Swift J1822.3–1606) – stars: neutron – X-rays: bursts – X-rays: general

Online-only material: color figures

1. INTRODUCTION

Over the past two decades, several new classes of neutron stars have been discovered (see Kaspi 2010 for a review). Perhaps the most exotic is that of the magnetars, which exhibit some highly unusual properties, often including violent outbursts and high persistent X-ray luminosities that exceed their spin-down powers (for reviews see Woods & Thompson 2006; Mereghetti 2008). These objects, while previously classified as anomalous X-ray pulsars (AXPs) and soft gamma repeaters (SGRs), are now generally accepted as a unified class of neutron stars powered by the decay of ultra-strong magnetic fields (e.g., Thompson et al. 2002).

To date, there are roughly two dozen magnetars and candidates observed,¹ with spin periods between 2 and 12 s, and high spin-down rates that generally suggest dipole B -fields of order 10^{14} – 10^{15} G (except SGR 0418+5729; Rea et al. 2010). Thanks to the *Swift* satellite, several new magnetars have been discovered in recent years via their outbursts (e.g., Rea et al. 2009; Göğüş et al. 2010; Kargaltsev et al. 2012). Once a new source has been identified, long-term monitoring is crucial to measure its timing properties, and hence to constrain the dipole magnetic field strength. Also, the flux evolution following an outburst could provide insights into many physical properties, such as the location of energy deposition during an outburst, the crust thickness, and heat capacity (see Pons & Rea 2012; A. Cumming et al., in preparation), or the physics of a highly active magnetosphere (Beloborodov 2009; Parfrey et al. 2012).

One of the latest additions to the list of magnetars is Swift J1822.3–1606. This source was first detected by *Swift* Burst Alert Telescope (BAT) on 2011 July 14 (MJD 55756) via its bursting activities (Cummings et al. 2011). It was soon identified as a new magnetar upon the detection of a pulse period $P = 8.4377 \text{ s}$ (Göğüş et al. 2011). No optical counterpart was

found, with 3σ limit down to a z -band magnitude of 22.2 (Rea et al. 2011). In Livingstone et al. (2011, hereafter Paper I), we reported initial timing and spectroscopic results using follow-up X-ray observations from *Swift*, the *Rossi X-ray Timing Explorer* (RXTE), and the *Chandra X-ray Observatory*. We found a spin-down rate of $\dot{P} = 2.54 \times 10^{-13}$ which implies a surface dipole magnetic field² $B = 4.7 \times 10^{13} \text{ G}$, the second lowest B -field among magnetars. Using an additional six months of *Swift* and *XMM-Newton* data, Rea et al. (2012) present a timing solution and spectral analysis. They find a spin-down rate of $\dot{P} = 8.3 \times 10^{-14}$, which implies a magnetic field of $B = 2.7 \times 10^{13}$, slightly lower than that found in Paper I.

In this paper, we present an updated timing solution, and the latest flux evolution using new observations from the same X-ray instruments as in Paper I. The additional two *Chandra* and 18 *Swift* observations provide a timing baseline that is over four times longer and allows a detailed study of the flux decay. We also report on an archival *ROSAT* observation to constrain the pre-outburst flux. We discuss the effects of timing noise on our timing solution and the properties and implications of this outburst within the magnetar model.

2. OBSERVATIONS

2.1. Swift Observations

The *Swift* X-Ray Telescope (XRT) consists of a Wolter-I telescope and an *XMM-Newton* EPIC-MOS CCD detector (Burrows et al. 2005). *Swift* is optimized to provide rapid follow-up of gamma-ray bursts and other X-ray transients. Following the 2011 July 14 outburst of Swift J1822.3–1606, the XRT was used to obtain 46 observations for a total exposure time of 175 ks. Data were collected in two different modes: photon counting (PC) and windowed timing (WT). While the former gives full imaging capability with a time resolution of 2.5 s, the

¹ See the magnetar catalog at <http://www.physics.mcgill.ca/~pulsar/magnetar/main.html>.

² The surface dipolar component of the B -field can be estimated by $B = 3.2 \times 10^{19} (P \dot{P})^{1/2} \text{ G}$.

latter forgoes imaging to provide 1.76 ms time resolution by reading out events in a collapsed one-dimensional strip.

For each observation, the unfiltered Level 1 data were downloaded from the *Swift* quicklook archive.³ For a summary of observations used, see Table 1. The standard XRT data reduction script, *xrtpipeline*, was then run using HEASOFT 6.11 and the *Swift* 20110725 CALDB. We reduced the events to the barycenter using the position of R.A. = 18^h22^m18^s, decl. = −16°04′26″8 (Pagani et al. 2011). Source and background events were extracted using the following regions: for WT mode, a 40 pixel long strip centered on the source was used to extract the source events and a strip of the same size positioned away from the source was used to extract the background events. For PC mode, a circular region with a radius of 20 pixels was used for the source region and an annulus with an inner radius of 40 pixels and an outer radius of 60 pixels was used as the background region. For the first PC mode observation (00032033001), a circular region with a radius of 6 pixels was excluded to avoid pileup. For the subsequent PC mode observation (00032033017), a region with a radius of 2 pixels was excluded. We estimate the maximum pileup fraction of the remaining PC observations be less than 5%.

For the spectral analysis, *Swift* ancillary response files, which provide the effective area as a function of energy, were created using the FTOOL *xrtmkarf* and the spectral redistribution matrices from the *Swift* CALDB were used.

2.2. RXTE Observations

The *RXTE* Proportional Counter Array (PCA) comprised five proportional counting units and provided a large collecting area and high timing precision (Jahoda et al. 2006). We downloaded 32 observations from the HEASARC archive spanning an MJD range from 55758 to 55893, for a total of 174 ks of integration time. The data were collected in GoodXenon mode, which records each event with 1 μ s time resolution. The observations are summarized in Table 1.

We selected events in the 2–10 keV energy range (PCA channels 6–14) from the top xenon layer of each Proportional Counter Unit (PCU) for our analysis, to maximize signal-to-noise ratio. The data from all the active PCUs were then merged. If more than one observation occurred in a 24 hr period, the observations were combined into a single data set. Photon arrival times were adjusted to the solar system barycenter using the same position as the for *Swift* data. Events were then binned into time series with resolution 1/32 s for use in the following analysis.

2.3. Chandra Observations

Following the outburst, we triggered our target of opportunity program with the *Chandra X-ray Observatory*. The telescope on board *Chandra* has an effective area ~ 3 times larger than that of *Swift* XRT, when used with the ACIS detector in continuous clocking (CC) mode. This mode has a time resolution of 2.85 ms and sensitivity between 0.3 and 10 keV.⁴ Five ACIS CC-mode observations were obtained between days 13 and 281 after the outburst, with exposures ranging from 10 to 20 ks. The observation parameters are summarized in Table 1. For imaging purposes, we also processed a short (1.2 ks) archival *Chandra* HRC-I observation taken 14 days after the outburst.

All *Chandra* data were processed using CIAO 4.3 with CALDB 4.4.6. We extracted the source events with a 6″ long strip region, and the remainder of the collapsed strip ($\sim 7'$ long), excluding the region within 1′ of the source in order to minimize any contamination from the wings of the point-spread function (PSF), was used for the background. We restricted the timing analysis to events between 0.3 and 8 keV. Photon arrival times were corrected to the solar system barycenter. The source spectrum was extracted using the tool *specextract*.

2.4. ROSAT Observation

The only existing X-ray image that covers the field prior to the outburst is a 6.5 ks *ROSAT* PSPC (Aschenbach 1985) observation of the nearby HII region M17 (Omega Nebula, G15.1–0.8). The observation has a time resolution of 130 ms. We downloaded the filtered event list from the HEASARC data archive⁵ and carried out the analysis using FTOOLS.

3. ANALYSIS AND RESULTS

3.1. Imaging

Figure 1 shows the *ROSAT* and *Chandra* images. *Swift* J1822.3–1606 is the only source detected in the *Chandra* HRC image and its radial profile is fully consistent with that of a model PSF. Hence, there is no evidence for any surrounding nebula or dust scattering halo. We find a source position of R.A. = 18^h22^m18^s.06, decl. = −16°04′25″.55 from the HRC image, which is consistent with the XRT position from Pagani et al. (2011) used above. We assume an error radius of 0′.6, which is the uncertainty in the absolute astrometry of *Chandra* for a 90% confidence interval.⁶ In the *ROSAT* image, an unresolved source is clearly detected at the position of the magnetar, as first reported by Esposito et al. (2011). Since the *Chandra* image shows no other bright X-ray sources in the field, we take this source to be *Swift* J1822.3–1606 in quiescence. Using a 4′ × 2′ elliptical aperture, we obtain 113 ± 11 total counts in 0.1–2.4 keV range, of which 48 ± 7 counts are due to background. Finally, we note that the diffuse X-ray emission $\sim 20'$ southwest of the magnetar is from M17, which contains the young stellar cluster NGC 6618 with over 100 OB stars (Lada et al. 1991).

3.2. Timing Analysis

3.2.1. Spin Evolution

Barycentered events were used to derive a pulse time-of-arrival (TOA) for each *Swift* WT mode, *RXTE*, and *Chandra* observation. For the *RXTE* observations, events were binned into time series with 31.25 ms resolution. The time series were then folded with 128 phase bins using the ephemeris from Paper I. A TOA was then measured from each profile by cross-correlation with a template profile. We verified that the *RXTE* pulse profiles were consistent with each other except in one isolated observation which was handled accordingly (see Section 3.2.2).

For *Swift* and *Chandra* observations, TOAs were extracted using a maximum likelihood (ML) method, as it yields more accurate TOAs than the traditional cross-correlation technique (see Livingstone et al. 2009). This method was not used for the *RXTE* observations as their high number of counts (due to the large collecting area and background count rates of

³ <http://swift.gsfc.nasa.gov/cgi-bin/sdc/q1>

⁴ <http://cxc.harvard.edu/proposer/POG/html/>

⁵ <http://heasarc.gsfc.nasa.gov/W3Browse/>

⁶ According to <http://cxc.harvard.edu/cal/ASPECT/celmon/>.

Table 1
Summary of Observations of Swift J1822.3–1606

ObsID	Mode	Obs. Date (yyyy-mm-dd)	MJD (TDB)	Exposure (ks)	Days Since Trigger
<i>Chandra</i>					
12612	ASIS-S CC	2011-07-27	55769.2	15.1	12.6
13511	HRC-I	2011-07-28	55770.8	1.2	14.2
12613	ASIS-S CC	2011-08-04	55777.1	13.5	20.5
12614	ASIS-S CC	2011-09-18	55822.7	10.1	66.1
12615	ASIS-S CC	2011-11-02	55867.1	16.3	110.5
14330	ASIS-S CC	2012-04-19	56036.9	20.0	280.4
<i>ROSAT</i>					
rp500311n00		1993-09-12	49242	6.7	...
<i>Swift</i>					
00032033001	PC	2011-07-15	55757.7	1.6	1.2
00032033002	WT	2011-07-16	55758.7	2.0	2.1
00032033003	WT	2011-07-17	55759.7	2.0	3.1
00032033005	WT	2011-07-19	55761.1	0.5	4.6
00032033006	WT	2011-07-20	55762.0	1.8	5.5
00032033007	WT	2011-07-21	55763.2	1.6	6.7
00032033008	WT	2011-07-23	55765.8	2.2	9.2
00032033009	WT	2011-07-24	55766.2	1.7	9.7
00032033010	WT	2011-07-27	55769.5	2.1	12.9
00032033011	WT	2011-07-28	55770.3	2.1	13.8
00032033012	WT	2011-07-29	55771.2	2.1	14.7
00032033013	WT	2011-07-30	55772.3	2.1	15.7
00032051001	WT	2011-08-05	55778.0	1.7	21.5
00032051002	WT	2011-08-06	55779.0	1.7	22.5
00032051003	WT	2011-08-07	55780.4	2.3	23.9
00032051004	WT	2011-08-08	55781.4	2.3	24.8
00032051005	WT	2011-08-13	55786.4	2.2	29.8
00032051006	WT	2011-08-14	55787.6	2.2	31.0
00032051007	WT	2011-08-15	55788.1	2.3	31.6
00032051008	WT	2011-08-16	55789.5	2.2	32.9
00032051009	WT	2011-08-17	55790.3	2.2	33.8
00032033015	WT	2011-08-27	55800.8	2.9	44.2
00032033016	WT	2011-09-03	55807.2	2.4	50.6
00032033017	PC	2011-09-18	55822.7	4.9	66.2
00032033018	WT	2011-09-20	55824.5	1.5	68.0
00032033019	WT	2011-09-25	55829.1	2.3	72.6
00032033020	WT	2011-10-01	55835.1	2.6	78.5
00032033021	WT	2011-10-07	55841.7	4.2	85.2
00032033022	WT	2011-10-15	55849.2	3.4	92.7
00032033023	WT	2011-10-22	55856.2	2.2	99.7
00032033024	PC	2011-10-28	55862.2	10.2	105.6
00032033025	PC	2012-02-19	55976.4	6.2	219.8
00032033026	WT	2012-02-20	55977.0	10.2	220.5
00032033027	PC	2012-02-21	55978.1	11.0	221.6
00032033028	WT	2012-02-24	55981.9	6.7	225.4
00032033029	WT	2012-02-25	55982.8	7.0	226.3
00032033030	WT	2012-02-28	55985.0	7.0	228.5
00032033031	WT	2012-03-05	55991.1	6.8	234.5
00032033032	WT	2012-04-14	56031.1	4.3	274.6
00032033033	WT	2012-05-05	56052.6	5.1	296.0
00032033034	WT	2012-05-26	56073.0	4.9	316.5
00032033035	WT	2012-06-17	56095.5	5.6	338.9
00032033036	WT	2012-06-26	56104.1	6.2	347.6
00032033037	WT	2012-07-06	56114.2	6.8	357.6
00032033039	WT	2012-08-17	56156.1	4.9	399.6
00032033040	WT	2012-08-22	56161.5	5.0	405.0
<i>RXTE</i>					
D96048-02-01-00		2011-07-16	55758.49	6.5	1.96
D96048-02-01-05		2011-07-18	55760.81	1.7	4.28
D96048-02-01-01		2011-07-19	55761.57	5.1	5.04
D96048-02-01-02		2011-07-20	55762.48	4.9	5.95
D96048-02-01-04		2011-07-21	55763.42	3.3	6.89

Table 1
(Continued)

ObsID	Mode	Obs. Date (yyyy-mm-dd)	MJD (TDB)	Exposure (ks)	Days Since Trigger
D96048-02-01-03		2011-07-21	55763.64	6.0	7.11
D96048-02-02-00		2011-07-22	55764.62	6.1	8.09
D96048-02-02-01		2011-07-23	55765.47	6.8	9.94
D96048-02-02-02		2011-07-25	55767.60	3.0	11.07
D96048-02-03-00		2011-07-29	55771.35	6.8	14.82
D96048-02-03-01		2011-08-01	55774.35	6.9	17.82
D96048-02-03-02		2011-08-04	55777.85	1.9	21.32
D96048-02-03-04		2011-08-04	55777.92	1.8	21.39
D96048-02-04-00		2011-08-07	55780.49	6.9	23.96
D96048-02-04-01		2011-08-09	55782.58	6.5	26.05
D96048-02-04-02		2011-08-11	55784.97	3.7	28.44
D96048-02-05-02		2011-08-12	55785.03	3.3	28.50
D96048-02-05-00		2011-08-15	55788.05	5.9	31.52
D96048-02-05-01		2011-08-16	55789.96	6.0	33.43
D96048-02-06-00		2011-08-21	55794.46	6.6	37.93
D96048-02-07-00		2011-08-26	55799.61	6.8	43.1
D96048-02-08-00		2011-09-06	55810.38	6.0	53.8
D96048-02-10-00		2011-09-16	55820.24	6.7	63.7
D96048-02-10-01		2011-09-22	55826.18	5.6	69.6
D96048-02-09-00		2011-09-25	55829.38	6.2	72.8
D96048-02-11-00		2011-10-01	55835.90	7.1	79.4
D96048-02-12-00		2011-10-08	55842.23	5.9	85.7
D96048-02-13-00		2011-10-15	55849.67	5.6	93.1
D96048-02-14-00		2011-10-29	55863.11	6.7	106.6
D96048-02-16-00		2011-11-13	55878.90	5.9	122.4
D96048-02-17-00		2011-11-20	55885.21	6.0	128.7
D96048-02-15-00		2011-11-28	55893.18	6.7	136.6

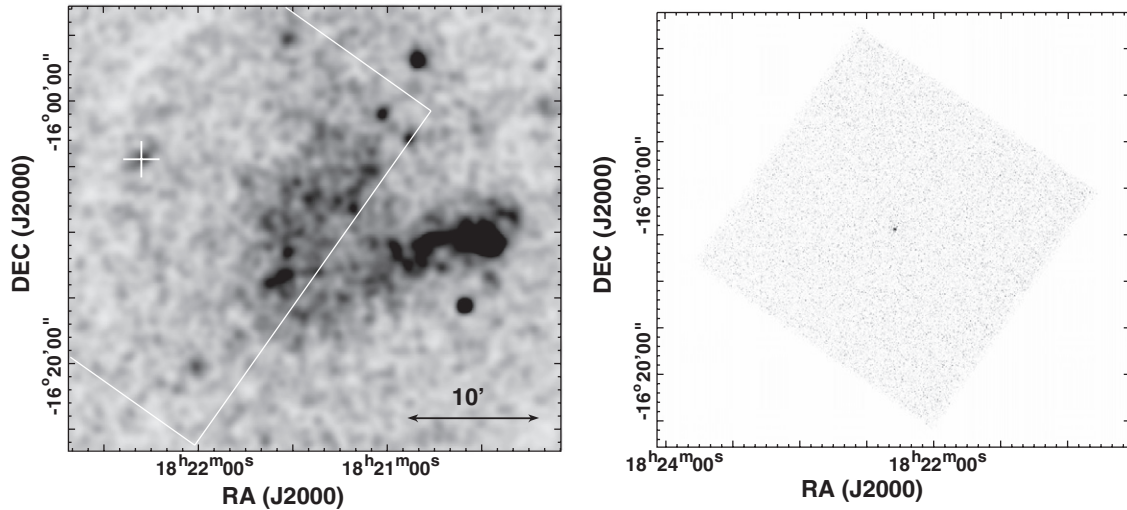


Figure 1. Left: *ROSAT* image of the field of Swift J1822.3–1606 in 0.1–2.4 keV range. The position of Swift J1822.3–1606 is marked by the cross, and the lines indicate the *Chandra* HRC observation field of view. The large-scale diffuse emission is the Galactic HII region M17. Right: 1.2 ks *Chandra* HRC exposure of Swift J1822.3–1606. Swift J1822.3–1606 is the only source detected.

the PCA) makes the ML method computationally expensive. The ML method for measuring TOAs requires a continuous model of the template pulse profile for which we used a Fourier model. The discrete Fourier transform of the binned template profile was first calculated. The template was then fitted by $f(\phi) = \sum_{j=0}^n \alpha_j e^{i2\pi j\phi}$, where α_j is the Fourier coefficient for the j th harmonic and ϕ is the phase between 0 and 1. The number of harmonics used was optimized to account for the features of the light curve while ignoring small fluctuations caused by the finite number of counts. For Swift J1822.3–1606, we used five harmonics to derive the TOAs.

For each observation, a probability or likelihood for a grid of trial offsets, ϕ_{off} , can be calculated using $P(\phi_{\text{off}}) = \prod_{i=0}^N f(\phi_i - \phi_{\text{off}})$, where ϕ_i is the phase of each photon folded at the best ephemeris of the pulsar. The likelihood distribution that results then describes the probability density for the average pulse arrival time. A TOA can be calculated from the optimal phase offset. We estimated TOA uncertainties by simulating 100 sets of events drawn from the pulse profile of the observation and measured an offset for each set using the ML method. The standard deviation of the simulated offset distribution was then taken as the TOA uncertainty. The ML derived TOAs

Table 2
Spin Parameters for Swift J1822.3–1606

Parameter	Value
Dates (Modified Julian Day)	55759–56161
Epoch (Modified Julian Day)	55761.0
Number of TOAs— <i>RXTE</i>	31
Number of TOAs— <i>Swift</i>	40
Number of TOAs— <i>Chandra</i>	5
Solution 1: one frequency derivative	
ν (s ⁻¹)	0.1185154253(3)
$\dot{\nu}$ (s ⁻²)	$-9.6(3) \times 10^{-16}$
rms residuals (ms)	52.2
χ^2_ν/ν	5.02/72
B (G)	$2.43(3) \times 10^{13}$
\dot{E} (erg s ⁻¹)	$4.5(1) \times 10^{30}$
τ_c (kyr)	1963(51)
Solution 2: two frequency derivatives	
ν (s ⁻¹)	0.1185154306(5)
$\dot{\nu}$ (s ⁻²)	$-2.4(1) \times 10^{-15}$
$\ddot{\nu}$ (s ⁻³)	$1.12(8) \times 10^{-22}$
rms residuals (ms)	32.2
χ^2_ν/ν	1.94/71
B (G)	$3.84(8) \times 10^{13}$
\dot{E} (erg s ⁻¹)	$1.12(5) \times 10^{31}$
τ_c (kyr)	784(33)
Solution 3: three frequency derivatives	
ν (s ⁻¹)	0.1185154343(8)
$\dot{\nu}$ (s ⁻²)	$-4.3(3) \times 10^{-15}$
$\ddot{\nu}$ (s ⁻³)	$4.4(6) \times 10^{-22}$
$\dddot{\nu}$ (s ⁻⁴)	$-2.2(4) \times 10^{-29}$
rms residuals (ms)	27.5
χ^2_ν/ν	1.44/70
B (G)	$5.1(2) \times 10^{13}$
\dot{E} (erg s ⁻¹)	$2.0(2) \times 10^{31}$
τ_c (kyr)	442(33)

Note. Errors are formal 1σ TEMPO uncertainties.

were consistent with those derived for Paper I using the cross-correlation method.

Timing solutions were then fit to the TOAs using TEMPO.⁷ Three solutions, one with a single frequency derivative, one with two frequency derivatives and one with three frequency derivatives, are given in Table 2. The top panel of Figure 2 shows the timing residuals with just ν and $\dot{\nu}$ fitted (Solution 1), the middle panel shows the residuals with $\ddot{\nu}$ also fitted (Solution 2), and the bottom panel shows the residuals with $\ddot{\nu}$ and $\dddot{\nu}$ also fitted (Solution 3). Solution 1 is a poor fit with a χ^2_ν/ν of 5.02/72. This is likely due to timing noise, a common phenomenon in young neutron stars including magnetars (e.g., Dib et al. 2008; Livingstone & Kaspi 2011). The best-fit ν and $\dot{\nu}$ values for Solution 1 imply a surface dipolar magnetic field of $B = 2.43 \pm 0.03 \times 10^{13}$ G. Solution 2, with a significant non-zero $\ddot{\nu}$, gives a better fit with a χ^2_ν/ν of 1.94/71. An F -test gives a probability of 2×10^{-16} that the addition of a second derivative does not significantly improve the fit. The surface dipolar magnetic field implied by Solution 2 is $B = 3.84 \pm 0.08 \times 10^{13}$ G. Solution 3, with a significant non-zero $\dddot{\nu}$, provides still a better fit than Solution 2 with a χ^2_ν/ν of 1.44/70. An F -test gives a probability of 3×10^{-6} that the addition of a third derivative does not significantly improve the

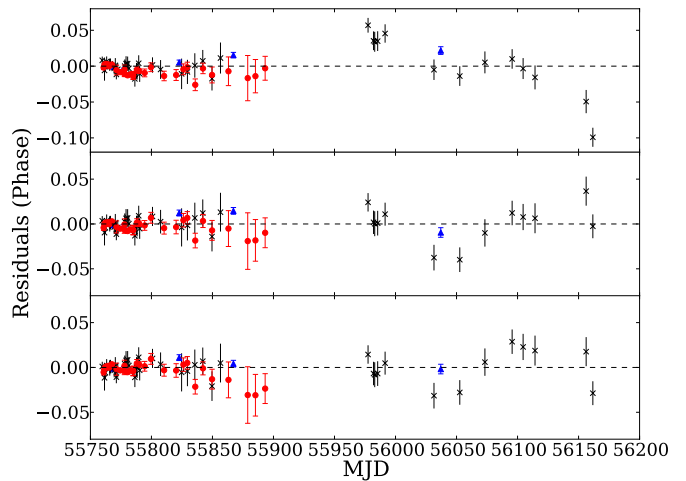


Figure 2. Timing residuals of Swift J1822.3–1606. The top panel shows the residuals for the timing solution with one frequency derivative (Solution 1); see Table 2. The middle panel shows the residuals with the addition of a second derivative (Solution 2). The bottom panel shows the residuals with three frequency derivatives fitted. *Swift* WT mode data are represented by crosses, red circles denote *RXTE* observations, and *Chandra* observations are shown as blue triangles.

(A color version of this figure is available in the online journal.)

fit. The best-fit parameters from Solution 3 imply a surface dipolar magnetic field of $B = 5.1 \pm 0.2 \times 10^{13}$ G.

Note that the fit is heavily influenced by the very high-quality *Chandra* TOAs. However, omitting them and including only TOAs from *Swift* and *RXTE* still yield significant second and third derivatives and an implied B -field of $B = 4.8 \pm 0.2 \times 10^{13}$ G, which is consistent with that of Solution 3. The above-quoted uncertainties in B and other derived quantities in Table 2 reflect only the statistical uncertainties in ν and its derivatives and do not include any contributions from the simplified assumptions in the standard formulae used to determine such quantities. Note that even with the addition of highly significant second and third derivatives, Solution 3 still does not provide an adequate fit. Adding additional derivatives reduces the χ^2 with marginal significance and results in larger values of the spin-down rate and hence B . For example, including a fourth frequency derivative does not result in significant improvement in χ^2 ($\chi^2_\nu/\nu = 1.31/69$) and yields $B = 6.0 \times 10^{13}$ G.

To search for pulsations in the *ROSAT* observation, we applied a barycenter correction to the event arrival times, then used the Z_m^2 test (Buccheri et al. 1983) to search for pulsations. We searched in the frequency range from zero to 3.8 kHz in steps of 1.3 μ Hz, oversampling the independent Fourier spacing by a factor of 10; however, we found no significant signal. By simulating a pulsar with a background subtracted count rate of that of the *ROSAT* observation, we find that the pulsar would be undetectable even with a pulsed fraction of 100%, and therefore we cannot constrain the pulsed fraction.

3.2.2. Pulse-profile Analysis

Here we search for time and energy variability in the pulse profile of Swift J1822.3–1606 using the *RXTE*, *Swift*, and *Chandra* observations. We created pulse profiles for each *RXTE* observation for energy ranges of 2–6 keV, 6–10 keV (with photons selected from only the top xenon layer), 10–15 keV, 15–20 keV, 20–40 keV, and 20–60 keV (with photons selected from all three xenon layers) using the Solution 2 ephemeris. For the *Chandra* data we produced pulse profiles with the

⁷ <http://www.atnf.csiro.au/people/pulsar/tempo/>

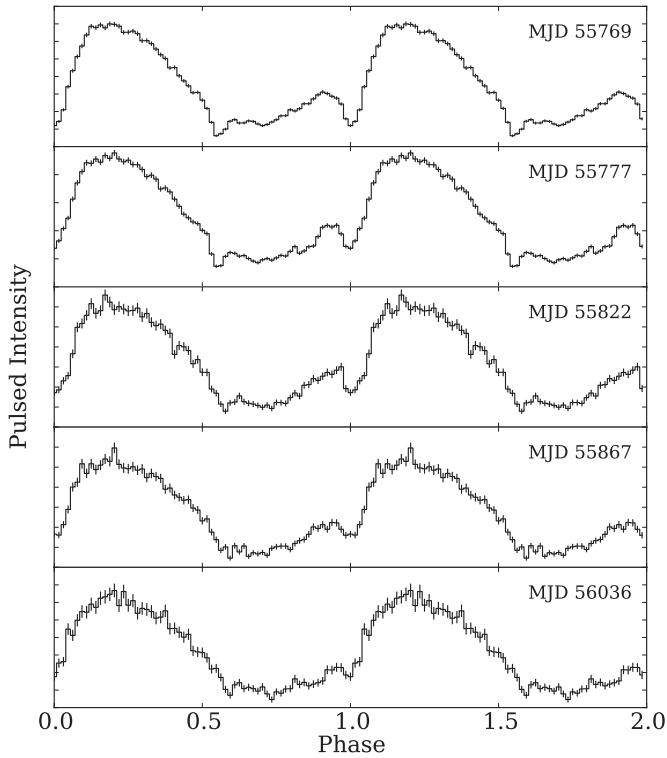


Figure 3. Pulse profiles with 64 bins from each of the four *Chandra* observations. The profiles are for the energy band 0.5–6 keV.

energy ranges of 0.5–6 keV, 0.5–2 keV, and 2–6 keV. For the *Swift* data we created 0.5–10 keV profiles, using only WT mode observations as PC mode does not have sufficient time resolution.

As in Paper I, we searched for time variability in pulse profiles but found that all the *RXTE* profiles are consistent with the template in each case except for the one profile from the very first observation after the outburst (ObsID D96048-02-01-00). The difference is due primarily to the off-pulse feature, which had slightly different structure between the template profile and the first *RXTE* observation. We therefore did not use D96048-02-01-00 in the timing analysis.

The *Chandra* profiles, however, do show evidence for low-level variability. Figure 3 shows the 0.5–6 keV pulse profile for each *Chandra* observation of Swift J1822.3–1606. We produced residuals between each pair of *Chandra* profiles by normalizing each profile and taking the difference between each normalized pair. A comparison of the profile residuals between each set of profiles shows that there is significant low-level evolution of the small “pulse” that precedes the main pulse. The main pulse does not exhibit any significant variation. The most significant variability is that between the first (MJD 55769) and last (MJD 56036) *Chandra* observation. The residuals between those two profiles have a χ^2_ν of 16.8 for 63 degrees of freedom. We note, however, that these low-level variations in the smaller component likely do not have a significant impact on the timing analysis, since the TOA extraction is heavily weighted toward the unchanging primary component. Indeed, our simulations of the effects of such low-level profile variations on the TOAs (see below) strongly support this conclusion.

The *Swift* profiles also show evidence for low-level variability. As above, we produced residuals between each pair of profiles and calculated a χ^2_ν for the null hypothesis. The measured values are not consistent with a χ^2 distribution, so there is significant

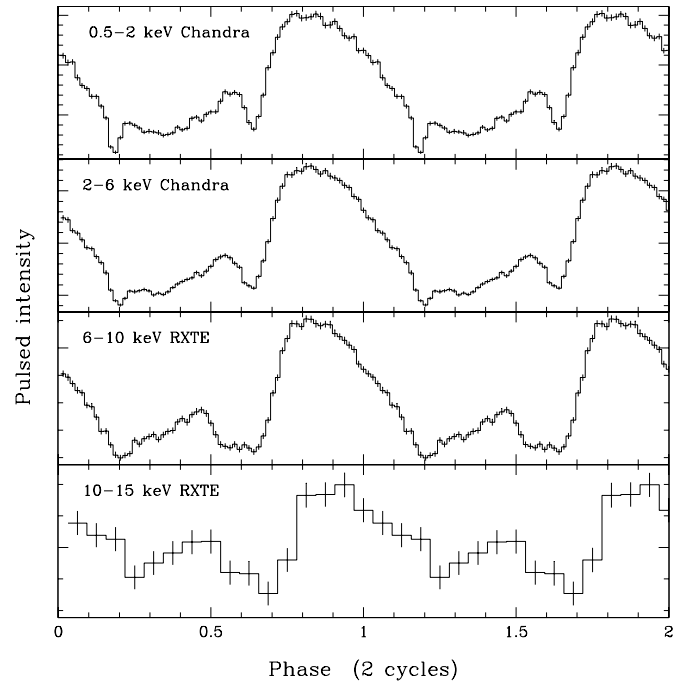


Figure 4. Pulse profiles for Swift J1822.3–1606 from *Chandra* and *RXTE* data for four energy ranges: 0.5–2 keV and 2–6 keV (*Chandra* data, 64 phase bins), and 6–10 keV and 10–15 keV (*RXTE* data, 64 and 16 phase bins).

variation between profile pairs. A closer look at the residuals shows that the variation is due primarily to the small interpulse, as in the *Chandra* data.

To investigate the dependence of pulse morphology on energy, we created a single high-significance profile by aligning and summing individual profiles for each energy range. Figure 4 shows a summary of the results, with the summed profiles for 0.5–2 keV (top panel, with 64 phase bins, *Chandra* data), 2–6 keV (middle panel, with 64 phase bins, *Chandra* data), 6–10 keV, and 10–15 keV (bottom two panels, *RXTE* data, with 64 and 16 phase bins, respectively). No pulsations were detected above 15 keV with the PCA. We then calculated residuals between pairs of profiles, and calculated χ^2_ν values of the resulting residuals in order to identify energy dependence of the pulse morphology. The most significant variability is between the 0.5–2 keV *Chandra* profile and the 6–10 keV *RXTE* profile. This can be seen in Figure 4 as a change in the phase of the interpulse, arriving later for higher energies. For this profile pair, the χ^2_ν of the residuals is 46.2 (for 28 degrees of freedom), excluding the null hypothesis. The interpulse variability causes significant differences between each pair of profiles, except the 10–15 keV profile, likely because of the lower statistics of the latter.

3.2.3. Comparison to Previously Reported Results

Rea et al. (2012) present a timing solution with a spin-down implied magnetic field of $B = 2.7 \times 10^{13}$ G. Their data set is similar to ours, although they use proprietary *XMM-Newton* data whereas we use proprietary *Chandra* data and our data set includes seven additional *Swift* observations. Their timing solution is similar to our Solution 1. They, however, do not find a significant second frequency derivative. A possible cause of this discrepancy could be the difference in TOA extraction methods. Instead of using a pulse-profile template, Rea et al. (2012) fit the folded profile for each observation with two sine functions with periods equal to the fundamental and the first harmonic of

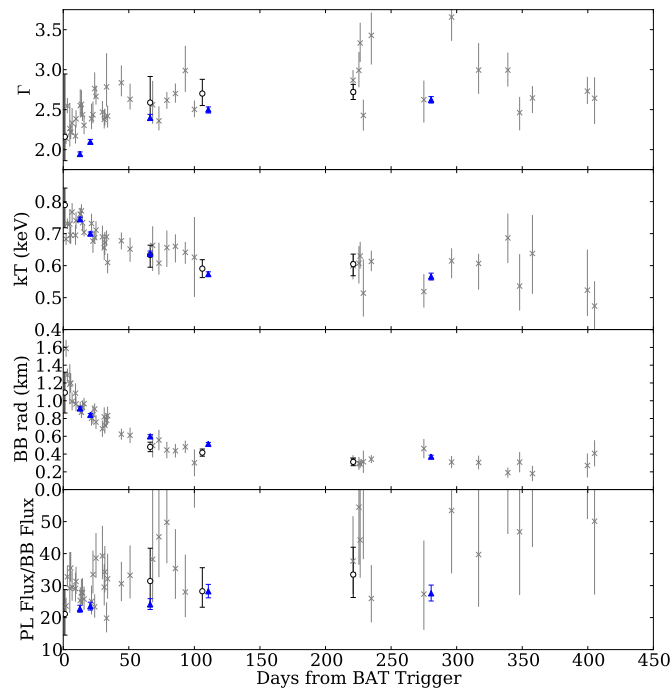


Figure 5. Spectral properties of Swift J1822.3–1606 following its outburst. Gray crosses represent *Swift* WT mode data, open circles are *Swift* PC mode data, and blue triangles denote *Chandra* observations. The determination of the blackbody radius assumes a distance of 1.6 kpc (see Section 4.3).

(A color version of this figure is available in the online journal.)

the pulse period. They then assign the ascending node of the fundamental sine function as the TOA of the pulse. This method was used to attempt to account for pulse-profile changes. We implemented this method and derived an additional set of TOAs to compare to our ML derived TOAs. We found that the sine-model-derived TOAs provided similar timing solutions as our ML TOAs and the addition of a second frequency derivative did significantly improve the fit, reducing the χ^2_ν/ν from 7.91/72 to 2.72/71. The addition of a third derivative in this case results in only marginal improvement with a χ^2_ν/ν of 2.47/70. If we limit our data set to the *Swift* and *RXTE* data used in Rea et al. (2012), we find that the addition of a second frequency derivative is not necessary, which is consistent with their findings.

In order to investigate the effects of pulse-profile changes on both TOA extraction methods, we simulated pulse profiles with an unchanging (other than noise) primary component and a varying secondary component, as is observed in the pulse-profile evolution of Swift J1822.3–1606. We modeled the profile using two Gaussians and modified the amplitude of the smaller Gaussian in order to vary the secondary component. We found that for both the sine-model and the ML methods, as the amplitude of the secondary component was varied, the measured phase offsets varied by less than their uncertainties. Hence, we conclude that the observed pulse-profile variations do not have an appreciable effect on the TOA determination, independent of which TOA extraction method was used.

3.3. Spectral Analysis and Flux Evolution

Spectral models were fit to the *Swift*, *Chandra*, and *ROSAT* data using XSPEC⁸ version 12.7. The quiescent flux of Swift J1822.3–1606 was determined by first extracting the source

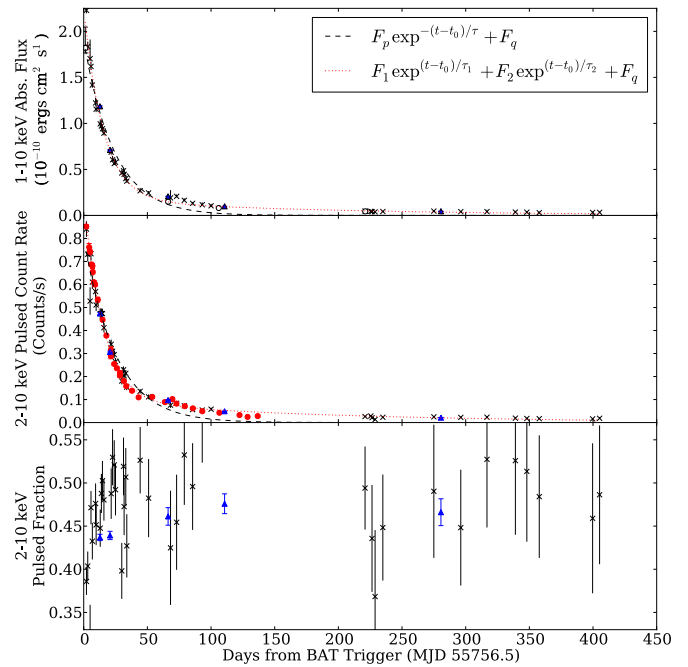


Figure 6. Flux evolution of Swift J1822.3–1606 following its outburst. The top panel shows the 1–10 keV absorbed flux as it decays. The middle panel shows that 2–10 keV pulsed count rate. The *RXTE*/PCA and *Chandra* count rates have been scaled to the *Swift* count rates by fitting overall scaling factors in the double-exponential fit. The bottom panel shows the pulsed fraction from *Swift* and *Chandra* observations. In all panels, *Swift* WT mode data are shown as gray crosses, *Swift* PC mode data are represented by open circles, *RXTE* data are shown as red circles, and data from *Chandra* are shown as blue triangles. The dotted lines show the result of the double-exponential fit to the total and pulsed flux decays, and the dashed line shows the results of the single-exponential fit.

(A color version of this figure is available in the online journal.)

spectrum from the *ROSAT* data, then fitting it with an absorbed blackbody model. The absorption column density N_H was fixed during the fit at the best-fit value ($4.53 \times 10^{21} \text{ cm}^{-2}$) determined from the *Swift* and *Chandra* spectra (see below). We obtained a quiescent blackbody temperature of $kT = 0.12 \pm 0.02 \text{ keV}$ and a radius of $5^{+7}_{-2} d_{1.6} \text{ km}$, where $d_{1.6}$ is the distance to the source in units of 1.6 kpc, the estimated distance as discussed in Section 4.3. We found an absorbed flux of $9^{+20}_{-9} \times 10^{-14} \text{ erg cm}^{-2} \text{ s}^{-1}$ in the 0.1–2.4 keV range.

The *Chandra* and *Swift* spectra were grouped with a minimum of 100 and 20 counts per bin, respectively. The spectra were fitted jointly to a photoelectrically absorbed blackbody model with an added power-law component. The model was fit with a single N_H using the XSPEC phabs model assuming abundances from Anders & Grevesse (1989) and photoelectric cross-sections from Bałucińska-Church & McCammon (1992). All the other parameters were allowed to vary from observation to observation.

The blackbody plus power-law model provided an acceptable fit to the *Swift* and *Chandra* data. The model had χ^2_ν/ν of 1.07/5451 and a best-fit N_H of $4.53 \pm 0.08 \times 10^{21} \text{ cm}^{-2}$. Figure 5 shows the evolution of the post-outburst spectral parameters. The spectrum is softening following the outburst as the 1–10 keV absorbed flux (top panel of Figure 6) decays: the photon index of the power-law component increases and the temperature of the blackbody decreases. This is clear from the high-quality *Chandra* data alone but is also apparent in the *Swift* data, and is consistent with the behavior of other magnetars post-outburst (see Section 4.2).

⁸ <http://xspec.gsfc.nasa.gov>

Table 3
Models of the Flux Evolution of Swift J1822.3–1606

Model	τ_1 (days)	τ_2 (days)	F_q (erg cm ⁻² s ⁻¹)	χ^2_ν
Single exponential	23.8 ± 0.5	...	3 × 10 ⁻¹⁴ (fixed)	20.1/43
Single exponential	19.5 ± 0.4	...	4.7 ± 0.2 × 10 ⁻¹²	4.48/42
Double exponential	15.5 ± 0.5	177 ± 14	3 × 10 ⁻¹⁴ (fixed)	2.17/41
Double exponential	9 ± 1	39 ± 3	4.0 ± 0.2 × 10 ⁻¹²	1.06/40

Figure 6 shows the flux decay and pulsed fraction evolution following the Swift J1822.3–1606 outburst. In Paper I, we showed that both a double-exponential model and an exponential model provided acceptable fits to both the total and pulsed flux decays, whereas a power-law decay model was excluded. Here we fitted a double-exponential decay and an exponential decay to the total and pulsed-flux evolutions. The exponential decay model is described by $F(t) = F_p \exp^{-(t-t_0)/\tau} + F_q$, where t is in MJD, F_p is the peak absorbed flux, F_q is the quiescent flux, t_0 is the time of the BAT trigger in MJD, and τ is decay timescale in days. The double-exponential decay is described by $F(t) = F_1 \exp^{-(t-t_0)/\tau_1} + F_2 \exp^{-(t-t_0)/\tau_2} + F_q$, where t_0 is the time of the BAT trigger in MJD, F_1 and F_2 are the absorbed fluxes at t_0 of each exponential component, and τ_1 and τ_2 are the decay timescales in days of each component. For both models we fit the data both by using the quiescent flux as a free parameter, and by using a fixed quiescent flux $F_q = 3 \times 10^{-14}$ erg cm⁻² s⁻¹. This is the approximate 1–10 keV flux assuming the 0.1–2.4 keV flux and spectral model from the *ROSAT* observation. Table 3 shows the results of these fits. With χ^2_ν of 1.06/40, the double-exponential decay with a free quiescent flux provides the best fit to the data. However, the best-fit value for the quiescent flux, $4.0 \pm 0.2 \times 10^{-12}$ erg cm⁻² s⁻¹, is more than two orders of magnitude higher than the quiescent flux implied by the *ROSAT* observation. We therefore take the double-exponential decay with the fixed quiescent flux as the best model of the total absorbed flux decay with timescales of $\tau_1 = 15.5 \pm 0.5$ days and $\tau_2 = 177 \pm 14$ days. In both cases, the single-exponential fit is much worse than the double exponential one.

In Figure 6, the absorbed flux measured with *Chandra* is always larger than that with *Swift* at a similar epoch by about 10%–15%. The discrepancy could be attributed to insufficient cross-calibration between instruments. Tsujimoto et al. (2011) found that flux measurements from different X-ray telescopes could differ by as much as 20%, and that *Chandra* appears to give a higher flux than others, as well as a harder photon index, which is consistent with our findings.

To determine the 2–10 keV pulsed count rate from *Swift*, *RXTE*, and *Chandra* observations, the barycentered events were folded using the Solution 2 ephemeris in Table 2 with 16 phase bins. For the *RXTE* observations, only data from the first xenon layer of PCU2 were used. Both PCU0 and PCU1 lost their propane layers and there is minimal PCU3 and PCU4 data for this source. The inclusion of only a single detector in the analysis reduces instrumental biases. For observations from all three telescopes, the pulsed count rate was then measured from each folded profile using an rms method as described in Dib et al. (2008), where the pulsed count rate, F , is given by

$$F = \sqrt{2 \sum_{k=1}^n [(a_k^2 + b_k^2) - (\sigma_{a_k}^2 + \sigma_{b_k}^2)]}, \quad (1)$$

where a_k is the even Fourier component and is equal to $(1/N) \sum_{i=1}^N p_i \cos(2\pi k i/N)$, σ_{a_k} is the uncertainty in a_k , b_k is the odd Fourier component and is equal to $(1/N) \sum_{i=1}^N p_i \sin(2\pi k i/N)$, σ_{b_k} is the uncertainty in b_k , i is an index over phase bins, N is the total number of phase bins, p_i is the count rate in the i th phase bin, and n is the maximum number of Fourier harmonics used. In this case, $n = 5$. This technique is equivalent to the simple rms formula, $F = (1/\sqrt{N})[\sum_{i=1}^N (p_i - \bar{p})^2]^{1/2}$, except only statistically significant Fourier components are used and the upward statistical bias is removed by subtracting the variances (Dib et al. 2008). For *Swift* and *Chandra* observations, pulsed fractions were determined by dividing the pulsed count rate by the total count rate.

The middle panel of Figure 6 shows the 2–10 keV pulsed-flux evolution of Swift J1822.3–1606. The pulsed count rates measured by each instrument depend on the different instrumental responses. The *RXTE* PCA and *Chandra* pulsed count rates were therefore scaled to the *Swift* WT mode values by including factors between each data set as free parameters in the double and single-exponential fits. For the pulsed-flux evolution, the double-exponential fit also provided the best fit with χ^2_ν of 5.15/74 and decay timescales of $\tau_1 = 15.3 \pm 0.2$ days and $\tau_2 = 182 \pm 6$ days. The exponential model had a χ^2_ν of 60.5/76 with a best-fit decay timescale of 25.1 ± 0.2 days. This is the opposite of what we found in Paper I where the exponential model was a better fit to the data available at the time.

3.4. X-Ray Bursts

To search for X-ray bursts in *RXTE* data of Swift J1822.3–1606, we created a time series for each active PCU from GoodXenon data for each observation, selecting events in the 2–20 keV range (PCA channels 6–24) and from all three detection layers (the same energy range as selected for similar searches for X-ray bursts from magnetars, e.g., Göğüş et al. 2001; Gavril et al. 2004). For the *Swift* observations, binned time series were made for each Good Timing Interval (GTI) in an observation. For both *Swift* and *RXTE*, time series were made at 15.625 ms, 31.25 ms, 62.5 ms and 125 ms time resolutions to provide sensitivity to bursts on a hierarchy of timescales.

Bursts were identified by comparing the count rate in the i th bin to the average count rate as described in Gavril et al. (2004). Because the background rate of the PCA typically varies over a single observation, we calculated a local mean around the i th bin for *RXTE*. For *Swift* data, a mean was calculated for each GTI. We then compared the count rate in the i th bin to the mean. If the count rate in a single bin was larger than the local/GTI average, the probability of such a count rate occurring by chance was calculated. For *RXTE* data, the probability of the count rate in the corresponding bin in the other active PCUs was also calculated (whether or not the count rate in that bin was greater than the local average). If a PCU was off during the bin of interest, its probability was set to 1. We then found the total probability that a burst was observed, by multiplying the probabilities for each PCU together. If the total probability of an event was $P_{i,\text{tot}} \leq 0.01/N$ (where N is the total number of time bins searched), it was flagged as a burst.

We found six bursts in *RXTE* data of Swift J1822.3–1606. The burst properties are summarized in Table 4. In the table are the MJDs of each burst, the number of counts in a 31.25 ms bin, and the probability that the burst would occur by chance given the local mean count rate. An insufficient number of bursts was detected to perform a detailed statistical analysis of the burst

Table 4
X-ray Bursts from Swift J1822.3–1606

<i>RXTE</i> ObsID	MJD	Total Counts	Chance Probability ^a
<i>RXTE</i> bursts			
D96048-02-01-01	55761.53224	15 ± 4	7.8×10^{-7}
D96048-02-01-01	55761.57082	36 ± 6	8.6×10^{-33}
D96048-02-01-02	55762.49919	21 ± 5	1.1×10^{-13}
D96048-02-03-04	55777.91627	12 ± 3	4.5×10^{-5}
D96048-02-04-01	55782.53122	13 ± 4	2.4×10^{-5}
D96048-02-05-01	55789.96209	11 ± 3	2.2×10^{-4}

Note. ^a The probability of the detected signal being due to noise.

properties for Swift J1822.3–1606. The bursts found were very narrow, typically only one or two 31.25 ms bins wide, and not very fluent compared to typical magnetar bursts (see Göğüş et al. 2001; Gavril et al. 2004; Scholz & Kaspi 2011; Lin et al. 2011). No significant changes in the long-term flux decay were observed at the times of these bursts.

Although in certain *Swift* observations we detected several bursts, these had much softer spectra than typical magnetar bursts and were also seen in the background region. Therefore, we do not believe that they originate from Swift J1822.3–1606. No other bursts were detected in any of the *Swift* data.

4. DISCUSSION

We have presented *Swift*, *RXTE*, *Chandra* observations following the discovery of Swift J1822.3–1606 during its outburst in 2011 July. We presented a phase-connected timing solution which suggests a spin-down inferred $B \sim 5 \times 10^{13}$ G, the second lowest measured for a magnetar thus far, although we note that timing noise may significantly contaminate this estimate. The flux of the magnetar was found to be decaying, both in total and pulsed flux, according to a double-exponential model. The spectrum softened following the outburst. Swift J1822.3–1606 also emitted several short bursts during its period of outburst. We also analyzed an archival *ROSAT* observation from which Esposito et al. (2011) previously reported that Swift J1822.3–1606 is detected in quiescence. We note that the source had a similar absorption column density to the nearby Galactic HII region M17. In the following we discuss the above results.

4.1. Timing Behavior

In Section 3.2 we presented a timing solution for Swift J1822.3–1606 with just ν and $\dot{\nu}$ fitted (Solution 1). However, this solution appears significantly contaminated by timing noise, a common phenomenon in pulsars. Most pulsars seem to display some unexplained “wandering” in their spin evolution (Hobbs et al. 2010). A measure of the amount of timing noise displayed by a pulsar is Δ_8 and is defined as $\Delta_8 = \log[(1/6\nu)|\dot{\nu}|(10^8\text{s})^3]$ (Arzoumanian et al. 1994). Hobbs et al. (2010) measured a correlation between \dot{P} and Δ_8 using timing solutions for 366 rotation-powered pulsars. Magnetars are very noisy timers, generally having more timing noise, as measured by Δ_8 , than those rotation-powered pulsars of similar properties (Gavril & Kaspi 2002; Woods et al. 2002). Here, for Swift J1822.3–1606, we measure $\Delta_8 = 2.8$ (using $\dot{\nu}$ from Solution 3), which is much higher than the value predicted from the correlation in Hobbs et al. (2010) of ~ -2 . However, we caution that in general the $\dot{\nu}$ used to calculate Δ_8 is measured for a data span of 10^8 s, whereas our data span is much shorter. The large value of Δ_8 we measured may be biased by the short span, or by unmodeled relaxation

following a hypothetical glitch that could have occurred at the BAT trigger. Glitches are commonly seen to accompany radiative outbursts from magnetars (e.g., Kaspi et al. 2003; Dib et al. 2009).

Due to the presence of timing noise, we take the timing and derived parameters of Solution 3 not as the “true” spin-inferred values, but as a “best guess” given the data thus far. As such, the uncertainties in the parameters presented, which do not take into account the effect of contamination by timing noise, likely underestimate the true uncertainties. Further timing observations of Swift J1822.3–1606 will help to average over the effects of timing noise and thus provide improved estimates of the spin-inferred magnetic field of the pulsar.

The B -field measured by Solution 1 would be the second-lowest measured for a magnetar to date, higher than only SGR 0418+5729 (Rea et al. 2010). Solution 3, although still the second-lowest yet measured, gives a higher value of B that is close to that of magnetar 1E 2259+586 and the magnetically active rotation-powered pulsar PSR J1846–0258. It is also similar to the quantum critical field of $B_{\text{QED}} = 4.4 \times 10^{13}$ G (Thompson & Duncan 1996) which has been viewed in the past of being a lower limit on the magnetic field of magnetars, although SGR 0418+5729 has shown that it is not a necessary condition for magnetar-like activity.

4.2. Flux and Spectral Evolution

In the twisted-magnetosphere model of magnetars, the thermal emission is thought to originate from heating within the star, caused by the decay of strong internal magnetic fields (Thompson et al. 2002). Currents in the magnetosphere, which are due to twists in the magnetic field (Thompson et al. 2002; Beloborodov 2009), scatter the thermal surface photons to higher energies. In addition to scattering, the currents provide a source of surface heating in the form of a return current. The flux increase that accompanies a magnetar outburst is theorized to be due a rapid heating which could originate from magnetospheric, internal, or crustal reconfiguration of the neutron star. This release may result in a significant increase in the surface temperature, in the return-current heating, and in the twisting of the magnetic field. Thus, an increase in flux due to an internal heat release should result in an increase of the hardness of the emission. This hardness–flux correlation is in agreement with observations of several magnetars (Gotthelf & Halpern 2007; Tam et al. 2008; Zhu et al. 2008; Scholz & Kaspi 2011).

Scholz & Kaspi (2011) explored the hardness–flux correlation for magnetar outbursts by comparing the relation between fractional increase in 4–10/2–4 keV hardness ratio and fractional increase in 2–10 keV unabsorbed flux for six different outbursts in four different magnetars. We present a similar plot here in Figure 7 for Swift J1822.3–1606. Here, however, the hardnesses and fluxes are absolute quantities and not fractional increases over quiescent values as in Scholz & Kaspi (2011), as there is no quiescent observation of Swift J1822.3–1606 with the appropriate spectral coverage. Figure 7 shows that Swift J1822.3–1606 softens as the flux decreases following the outburst and so is in broad agreement with the hardness–flux correlation observed in other magnetar outbursts. This spectral softening with flux decline is clear also in Figure 5, where kT declines and the power-law index Γ increases as the flux drops.

4.2.1. Magnetars in Quiescence

The quiescent flux of Swift J1822.3–1606 measured by *ROSAT* in 1993 is about three orders of magnitude lower than

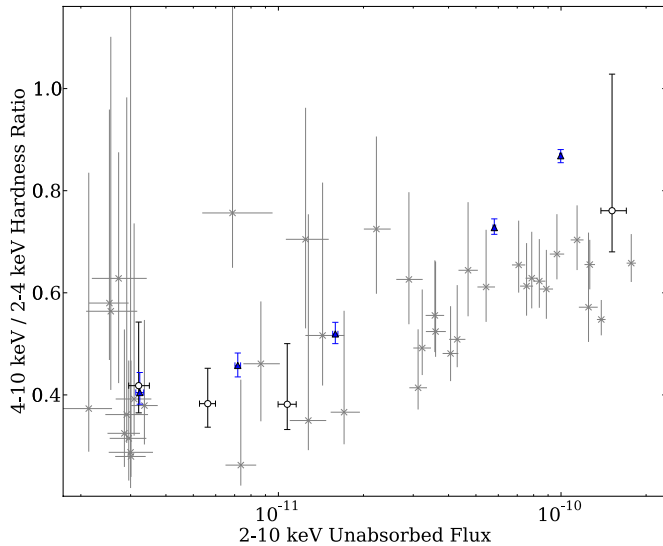


Figure 7. Spectral hardness as a function of unabsorbed flux for Swift J1822.3–1606. The *Swift* WT mode observations are shown as gray crosses, the *Swift* PC mode data are denoted by open circles, and the blue triangles represent the *Chandra* observations.

(A color version of this figure is available in the online journal.)

the peak flux measured following the outburst. Such large flux variations have been observed in several other magnetars (e.g., 1E 1547–5408, XTE J1810–197 and AX J1845–0258; Ibrahim et al. 2004; Gotthelf et al. 2004; Tam et al. 2006; Scholz & Kaspi 2011; Bernardini et al. 2011). Other magnetars, such as 1E 1841–045 (Zhu & Kaspi 2010; Lin et al. 2011), 4U 0142+61 (Gonzalez et al. 2010), and 1RXS J170849.0–400910 (den Hartog et al. 2008) have not exhibited large flux variations, but are much brighter in quiescence than are the magnetars with large outbursts. The cause of this difference is unclear. Pons & Rea (2012) suggest that there is a maximum luminosity that can be reached by a magnetar during an outburst due to neutrino cooling dominating at high crust temperatures. This helps to explain the differences in outburst magnitudes, but does not address the wide range of quiescent luminosities.

Case in point, the magnetar 1E 2259+586 has spin properties that are likely quite similar to those of Swift J1822.3–1606 but has a much higher quiescent luminosity. The magnetic field measured from spin-down for 1E 2259+586 is 5.9×10^{13} G (Gavril & Kaspi 2002), close to $B = 5.1 \times 10^{13}$ G for Swift J1822.3–1606 as estimated by our Solution 3. 1E 2259+586 also went into a period of outburst on 2002 June 18 where the flux increased by a factor of $\gtrsim 20$ (Woods et al. 2004). However, in quiescence, 1E 2259+586 is much brighter than Swift J1822.3–1606 with a quiescent 2–10 keV luminosity of 2×10^{34} erg s $^{-1}$ (Zhu et al. 2008) compared to $\lesssim 10^{31}$ erg s $^{-1}$ for Swift J1822.3–1606.

One possibility is that the “true” magnetic fields of the more luminous magnetars are higher than those of the fainter magnetars. The spin-down of the neutron star is only sensitive to the dipole component of the magnetic field. If the magnetic field had significant components in higher multipoles or a toroidal component (Thompson & Duncan 1996; Pons & Perna 2011), the true magnetic field could be higher.

Another possibility is that neutrino cooling in the core is setting a long-term luminosity limit, and that the neutrino cooling properties of the stars are different, e.g., due to different masses. For example, consider first the case where the neutrino

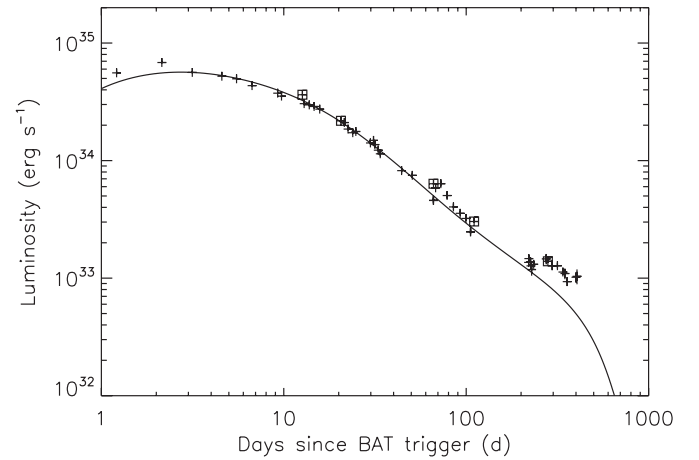


Figure 8. Model of the thermal relaxation of the neutron-star crust that approximately reproduces the observed 1–10 keV luminosity decay assuming a distance of 1.6 kpc. In the model, we deposit an energy 3×10^{42} ergs in the outer crust between densities of 2×10^9 – 3×10^{10} g cm $^{-3}$. The subsequent cooling of the crust gives a good match to the observed light curve.

emission in the core is due to the modified URCA process, with an emissivity $\epsilon_v \sim 10^{20}$ erg cm $^{-3}$ s $^{-1}$ T_9^8 (Yakovlev et al. 2003). If we take the magnetic-field decay time to be $\tau = 10^4$ yr, then the luminosity from magnetic field decay is roughly $L_B = (B^2/8\pi)(4\pi R^3/3)(1/\tau) = 10^{34}$ erg s $^{-1}$ for $B = 10^{14}$ G. Balancing this with the neutrino losses $L_v = (4\pi R^3/3)\epsilon_v$, we find a core temperature $T_c = 2.5 \times 10^8$ K or, using the core temperature–luminosity relation from Potekhin & Yakovlev (2001), a luminosity $L \approx 4 \times 10^{33}$ erg s $^{-1}$. On the other hand, if the neutrino emission is by the direct URCA process, with $\epsilon_v \sim 10^{26}$ erg cm $^{-3}$ s $^{-1}$ T_9^6 (Yakovlev et al. 2003), we find a core temperature $T_c = 1.5 \times 10^7$ K, corresponding to a surface luminosity of $\approx 2 \times 10^{31}$ erg s $^{-1}$. This shows that we might reasonably expect a factor of $\gtrsim 200$ in luminosity between different stars if one has slow neutrino emission in the core, and the other fast, for example, if the mass of one of the stars is large enough for direct URCA reactions to occur in the core. Even in the case where external currents dominate the quiescent luminosity, thermal emission from the neutron star provides a baseline luminosity, so that the low quiescent luminosity of Swift J1822.3–1606 suggests a low core temperature which implies either a low heating rate or efficient neutrino emission.

4.2.2. The Observed Luminosity Decay of Swift J1822.3–1606

We find that the observed luminosity decay is well reproduced by models of thermal relaxation of the neutron-star crust following the outburst. An example is shown in Figure 8, which shows the cooling of the crust after an injection of $\approx 3 \times 10^{42}$ ergs of energy at low density $\approx 10^{10}$ g cm $^{-3}$ in the outer crust at the start of the outburst. We follow the evolution of the crust temperature profile by integrating the thermal diffusion equation. The calculation and microphysics follow Brown & Cumming (2009) who studied transiently accreting neutron stars, but with the effects of strong magnetic fields on the thermal conductivity included (Potekhin et al. 1999) and for the outer boundary condition using the $T_{\text{eff}}-T_{\text{int}}$ relation appropriate for a magnetized envelope following Potekhin & Yakovlev (2001). The calculation follows the radial structure only; we assume that the magnetic field geometry is a dipole and take appropriate spherical averages to account for the variation in thermal conductivity across the star (Potekhin et al. 1999).

We assume $B = 6 \times 10^{13}$ G, similar to the value inferred from the spin-down, a $1.6 M_{\odot}$, $R = 11.2$ km neutron star, and take an impurity parameter for the inner crust of $Q_{\text{imp}} = 10$ (Jones 2004). We set the neutron-star core temperature to 2×10^7 K, which is needed to obtain a quiescent luminosity $< 10^{32}$ erg s $^{-1}$.

With the neutron-star parameters fixed, we then vary the location and strength of the heating and find that we obtain good agreement with the observed light curve for times < 100 days, if the initial heating event is located at low densities $\lesssim 3 \times 10^{10}$ g cm $^{-3}$. This conclusion comes from matching the observed timescale of the decay, and is not very sensitive to the choice of neutron-star parameters. For example, changing the neutron-star gravity changes the crust thickness and therefore cooling time, giving an inferred maximum density $\rho_{\text{max}} \propto g^{-2}$. This means that the inferred density can change by a factor of a few but cannot be moved into the neutron drip region, for instance. That only a shallow part of the outer crust is heated is an interesting constraint on models of crust heating in a magnetar outburst. We find that it is difficult to match the observed light curve at times $\gtrsim 200$ days, but the late-time behavior of the light curve is sensitive to a number of physics inputs associated with the inner crust, including the thermal conductivity and superfluid parameters, as well as modification due to the angular distribution of the heating over the surface of the star. We will investigate the late-time behavior in more detail in future work. Figure 8 suggests that the source could undergo significant further cooling in the coming years.

4.3. Distance Estimate and Possible Association

As shown in the *ROSAT* image (Figure 1), the Galactic HII region M17 is located $\sim 20'$ southwest of Swift J1822.3–1606. It has a distance of 1.6 ± 0.3 kpc (Nielbock et al. 2001) and an absorption column density $N_{\text{H}} = 4 \pm 1 \times 10^{21}$ cm $^{-2}$ (Townsend et al. 2003) which is consistent with our best-fit value of $4.53 \pm 0.08 \times 10^{21}$ cm $^{-2}$. This suggests that Swift J1822.3–1606 could have a comparable distance to that of M17.⁹ If so, then Swift J1822.3–1606 would be one of the closest magnetars detected thus far.

The above argument does not necessitate a direct association between M17 and Swift J1822.3–1606. However, if Swift J1822.3–1606 is associated with M17, then its angular separation of $26'$ from the cluster center, where the X-ray emission peaks in the *ROSAT* image, implies a physical distance of 12 pc. For a pulsar age of 10^5 yr, this requires a space velocity of only ~ 100 km s $^{-1}$ (corresponding to a proper motion of $0''.016$ yr $^{-1}$). This would make a direct proper motion measurement difficult. From timing, the characteristic age appears to be larger than 10^5 yr which would further reduce the implied proper motion. On the other hand, characteristic ages can be large overestimates of the true age. However, even if the true age were as low as 10^4 yr, the proper motion would be difficult to measure even with *Chandra*. Additionally, if the magnetar was born near an edge of the cluster, the angular separation from its birthplace could be larger or smaller by up to $\sim 10'$.

5. CONCLUSIONS

We have presented an analysis of the post-outburst radiative evolution and timing behavior of Swift J1822.3–1606, following its discovery on 2011 July 14. Following a timing analysis

for the source post-outburst, we estimate the surface dipolar component of the B -field to be $\sim 5 \times 10^{13}$ G, slightly higher than that inferred in Paper I. However, as this measurement is contaminated by timing noise, the true value of the magnetic field could be well outside of the uncertainties quoted in Table 2. Further monitoring of Swift J1822.3–1606 as it fades following the outburst will allow us to better account for the timing noise and measure more robust timing parameters.

The quiescent flux of Swift J1822.3–1606 measured using a 1993 *ROSAT* observation of M17 was found to be roughly three orders of magnitude lower than the peak flux during the outburst. The flux evolution following the outburst was well characterized by a double-exponential decay. By applying a crustal cooling model to the flux decay, we found that the energy deposition likely occurred in the outer crust at a density of $\sim 10^{10}$ g cm $^{-3}$. The spectral properties of Swift J1822.3–1606 were observed to soften following the outburst, with the power-law index increasing and the temperature of the blackbody decreasing. Indeed, a hardness–flux correlation, similar to what is observed in other magnetars, was clearly observed. Based on the similarity in N_{H} to that of the HII region M17, we argue for a source distance of 1.6 ± 0.3 kpc, one of the closest distances yet inferred for a magnetar.

We are grateful to the *Swift*, *Chandra*, and *RXTE* teams for their flexibility in scheduling TOO observations. We thank the anonymous referee for helpful comments and suggestions. V.M.K. holds the Lorne Trottier Chair in Astrophysics and Cosmology and a Canadian Research Chair in Observational Astrophysics. This work is supported by NSERC via a Discovery Grant, by FQRNT via the Centre de Recherche Astrophysique du Québec, by CIFAR, and a Killam Research Fellowship.

REFERENCES

- Anders, E., & Grevesse, N. 1989, *Geochim. Cosmochim. Acta*, **53**, 197
 Arzoumanian, Z., Nice, D. J., Taylor, J. H., & Thorsett, S. E. 1994, *ApJ*, **422**, 671
 Aschenbach, B. 1985, *Rep. Prog. Phys.*, **48**, 579
 Bałucińska-Church, M., & McCammon, D. 1992, *ApJ*, **400**, 699
 Beloborodov, A. M. 2009, *ApJ*, **703**, 1044
 Bernardini, F., Israel, G. L., Stella, L., et al. 2011, *A&A*, **529**, A19
 Brown, E. F., & Cumming, A. 2009, *ApJ*, **698**, 1020
 Bucccheri, R., Bennett, K., Bignami, G. F., et al. 1983, *A&A*, **128**, 245
 Burrows, D. N., Hill, J. E., Nousek, J. A., et al. 2005, *Space Sci. Rev.*, **120**, 165
 Cummings, J. R., Burrows, D., Campana, S., et al. 2011, *ATel*, **3488**, 1
 den Hartog, P. R., Kuiper, L., & Hermsen, W. 2008, *A&A*, **489**, 263
 Dib, R., Kaspi, V. M., & Gavril, F. P. 2008, *ApJ*, **673**, 1044
 Dib, R., Kaspi, V. M., & Gavril, F. P. 2009, *ApJ*, **702**, 614
 Esposito, P., Rea, N., Israel, G. L., & Tiengo, A. 2011, *ATel*, **3495**
 Göğüş, E., Kouveliotou, C., Woods, P. M., et al. 2001, *ApJ*, **558**, 228
 Gavril, F. P., & Kaspi, V. M. 2002, *ApJ*, **567**, 1067
 Gavril, F. P., Kaspi, V. M., & Woods, P. M. 2004, *ApJ*, **607**, 959
 Gonzalez, M. E., Dib, R., Kaspi, V. M., et al. 2010, *ApJ*, **716**, 1345
 Gotthelf, E. V., & Halpern, J. P. 2007, *ApJ*, **664**, L35
 Gotthelf, E. V., Halpern, J. P., Buxton, M., & Bailyn, C. 2004, *ApJ*, **605**, 368
 Göğüş, E., Cusumano, G., Levan, A. J., et al. 2010, *ApJ*, **718**, 331
 Göğüş, E., Kouveliotou, C., & Strohmayer, T. 2011, *ATel*, **3491**
 Hobbs, G., Lyne, A. G., & Kramer, M. 2010, *MNRAS*, **402**, 1027
 Ibrahim, A. I., Markwardt, C. B., Swank, J. H., et al. 2004, *ApJ*, **609**, L21
 Jahoda, K., Markwardt, C. B., Radeva, Y., et al. 2006, *ApJS*, **163**, 401
 Jones, P. B. 2004, *MNRAS*, **351**, 956
 Kargaltsev, O., Kouveliotou, C., Pavlov, G. G., et al. 2012, *ApJ*, **748**, 26
 Kaspi, V. M. 2010, *Proc. Natl Acad. Sci.*, **107**, 7147
 Kaspi, V. M., Gavril, F. P., Woods, P. M., et al. 2003, *ApJ*, **588**, L93
 Lada, C. J., Depoy, D. L., Merrill, K. M., & Gatley, I. 1991, *ApJ*, **374**, 533
 Lin, L., Kouveliotou, C., Göğüş, E., et al. 2011, *ApJ*, **740**, L16
 Livingstone, M. A., & Kaspi, V. M. 2011, *ApJ*, **742**, 31
 Livingstone, M. A., Ransom, S. M., Camilo, F., et al. 2009, *ApJ*, **706**, 1163

⁹ While there are two molecular clouds surrounding M17 (Wilson et al. 2003), they are confined to the north and west, such that they should not contribute to the N_{H} of either M17 or Swift J1822.3–1606.

- Livingstone, M. A., Scholz, P., Kaspi, V. M., Ng, C.-Y., & Gavriil, F. P. 2011, [ApJ](#), **743**, L38
- Mereghetti, S. 2008, [A&AR](#), **15**, 225
- Nielbock, M., Chini, R., Jütte, M., & Manthey, E. 2001, [A&A](#), **377**, 273
- Pagani, C., Beardmore, A. P., & Kennea, J. A. 2011, [ATel](#), 3493
- Parfrey, K., Beloborodov, A. M., & Hui, L. 2012, [ApJ](#), **754**, L12
- Pons, J. A., & Perna, R. 2011, [ApJ](#), **741**, 123
- Pons, J. A., & Rea, N. 2012, [ApJ](#), **750**, L6
- Potekhin, A. Y., Baiko, D. A., Haensel, P., & Yakovlev, D. G. 1999, [A&A](#), **346**, 345
- Potekhin, A. Y., & Yakovlev, D. G. 2001, [A&A](#), **374**, 213
- Rea, N., Esposito, P., Turolla, R., et al. 2010, [Science](#), **330**, 944
- Rea, N., Israel, G. L., Esposito, P., et al. 2012, [ApJ](#), **754**, 27
- Rea, N., Israel, G. L., Turolla, R., et al. 2009, [MNRAS](#), **396**, 2419
- Rea, N., Mignani, R. P., Israel, G. L., & Esposito, P. 2011, [ATel](#), 3515
- Scholz, P., & Kaspi, V. M. 2011, [ApJ](#), **739**, 94
- Tam, C. R., Gavriil, F. P., Dib, R., et al. 2008, [ApJ](#), **677**, 503
- Tam, C. R., Kaspi, V. M., Gaensler, B. M., & Gotthelf, E. V. 2006, [ApJ](#), **652**, 548
- Thompson, C., & Duncan, R. C. 1996, [ApJ](#), **473**, 322
- Thompson, C., Lyutikov, M., & Kulkarni, S. R. 2002, [ApJ](#), **574**, 332
- Townsley, L. K., Feigelson, E. D., Montmerle, T., et al. 2003, [ApJ](#), **593**, 874
- Tsujimoto, M., Guainazzi, M., Plucinsky, P. P., et al. 2011, [A&A](#), **525**, A25
- Wilson, T. L., Hanson, M. M., & Muters, D. 2003, [ApJ](#), **590**, 895
- Woods, P. M., Kaspi, V. M., Thompson, C., et al. 2004, [ApJ](#), **605**, 378
- Woods, P. M., Kouveliotou, C., Göğüş, E., et al. 2002, [ApJ](#), **576**, 381
- Woods, P. M., & Thompson, C. 2006, in *Compact Stellar X-ray Sources* ed. W. H. G. Lewin & M. van der Klis (Cambridge: Cambridge Univ. Press), 547
- Yakovlev, D. G., Levenfish, K. P., & Haensel, P. 2003, [A&A](#), **407**, 265
- Zhu, W., & Kaspi, V. M. 2010, [ApJ](#), **719**, 351
- Zhu, W., Kaspi, V. M., Dib, R., et al. 2008, [ApJ](#), **686**, 520